Numerical modeling of dust particle configurations in a cylindrical radio-frequency plasma reactor

M. Davoudabadi and F. Mashayek*

Department of Mechanical and Industrial Engineering, University of Illinois at Chicago, 842 West Taylor Street, Chicago, Illinois 60607, USA

(Received 12 August 2007; published 30 November 2007)

In the present work, first, plasma phase variables in a cylindrical radio-frequency (rf) plasma reactor are numerically solved using the local field approximation model. Then, equilibrium configurations of a few interacting (sub-)micron-sized dust particles are obtained by integrating the particles equations for their motion and charge, accounting for the various forces acting on each particle in a three-dimensional Lagrangian framework. Direct comparison of the results with experiment demonstrates excellent qualitative agreement. Based on the ion focus phenomenon, a physical model is formulated and proven successful in simulating the vertically aligned structures.

DOI: 10.1103/PhysRevE.76.056405 PACS number(s): 52.27.Lw, 52.80.Pi, 52.65.−y

I. INTRODUCTION

Confinement of a small number of (sub-)micron-sized particles within potential traps of laboratory nonequilibrium plasmas leads to various organized monolayer structures of the particles [1,2]. Under the conditions that the interparticle Coulomb energy greatly exceeds the particles thermal energy, a solidlike structure of plasma crystal is formed [3,4]. This situation is characterized by the Coulomb coupling parameter [3], $Q_p^m Q_p^n \exp(-k)/4\pi\epsilon_0 k_B T_p |\vec{r}_m - \vec{r}_n|$ becoming greater than the solidification limit. (In this definition, Q_p^m refers to the charge of the mth particle, k to the lattice parameter defined as $k=|\vec{r}_m-\vec{r}_n|/0.5(\lambda_D^m+\lambda_D^n)$ (with λ_D the local effective Debye length), ϵ_0 to the permittivity of free space, k_B to the Boltzmann constant, T_p to the particles temperature, and finally $\vec{r}$ to the particle distance [from the origin $(r,z,\theta)=(0,0,0)$] vector.) Increasing the number of particles causes the monolayer structure to become energetically less favorable and to transform into a multilayer crystal [5] with three-dimensional bcc, fcc, hcp, or quasi-two-dimensional vertically aligned hexagonal lattice structures [6–11].

Modeling the structures formed by a large count of particles submerged in the plasma involves numerous computational obstacles. First, as the number of particles increases [the Havnes parameter [12], $695 T_e(\mathrm{eV}) a_p(\mu m) n_p/n_e$, where T_e is the electron temperature, a_p the dust particle radius, and n_p and n_e dust particle and electron number density, respectively, exceeds a threshold value], particles electrostatic influence on the plasma structure becomes significant, and two-way coupling of the plasma and particles phases has to be carried out. In the locations where the charge density carried by the particle component is comparable to that of the electron and ion components, the charge on the neighboring particles affects the quasineutrality of the plasma. In the meantime, the "competition" of particles to absorb free charges results in a reduction of the electron charging current (i.e., "electron depletion" phenomenon) and eventually to a reduction of the particles potential with respect to the plasma potential in the dust cloud [13,14].

Furthermore, in the particle phase, calculation of particles interactions (i.e., N-body problem) adds another complexity in the regime of a dense particle phase. More restrictively, implications of the inherent multiscale temporal characteristic in the phenomenon under study makes the calculations prohibitively expensive from the computational cost standpoint. On one hand, the plasma phase macro time scale is that of the applied voltage period which is in the order of 10^{-7} s. On the other hand, the particles, with a typical radius of 1 μm, travel the interelectrode distance in a time scale of a tenth of a second which dictates the computational final time. Although due to their much smaller charge per mass (compared with the plasma particles), dust particles do not need to be moved at every plasma time step or even period, the computational load due to such a disparity of time scales raises a serious issue shadowing the feasibility of such a task, which is postponed to future studies.

More importantly, in order to accurately account for the effect of the plasma anisotropy around the particles (caused by either ions streaming effect or "closely packed" particles), the potential around the particle must be calculated in an adequately resolved manner. This requires the mesh size around the moving particle to be in the order of the particle size (nanometer-micron) and the particle to be regarded as an object with a definitive boundary. In the view that resolution of such a spatially multiscale problem with current computational power is obviously an impossible task, the implementation of models becomes imperative.

It is well-established that ions acceleration due to intense electric fields in the presheath leads to a directional disruption of the otherwise symmetric potential around the particles submerged in the sheath regions of plasma reactors. Amongst various complex mechanisms proposed [15–17], vertical alignment of the particles is commonly attributed to the ion focus region formed in the downstream side of the particles. Such a mechanism is frequently modeled by assuming a positive pointlike charge at a distance behind (with respect to the ion flow direction) the particle, and calculating the resulting monopole-monopole force on the other particle [18–23]. In the current work, motivated by the simple "dipole" model of binary particle-particle interactions intro-

*mashayek@uic.edu

duced by Yaroshenko *et al.* [24,25] we extend and formulate the model in the most general form. Relaxing numerous assumptions, we assume each particle with its corresponding ion focus region to be composed of one plasma shielded monopole and one plasma shielded dipole. Hence the total interaction between two particles will theoretically be a superposition of four interactions: a monopole-monopole interaction where the Debye-Huckel potential holds, a dipole-dipole interaction, and two monopole-dipole interactions. [By the virtue of assuming unshielded (vacuum-limit), equal, and parallel dipoles, Yaroshenko *et al.* account only for the first two, while presuming the ions flow in a vertical direction and that the two particles have equal charge.]

Numerical simulation of the plasma enhanced chemical vapor deposition (PECVD) process for coating of submicron-sized particles can help us understand the process and examine the possibilities of eliminating its drawbacks such as nonuniformity of the coating layer on the smaller particles [26]. Such a study provides insights also into particle contamination in PECVD reactors of the microelectronic industry. As a continuation of our study [27–30], we extend our simulations to the axisymmetric cylindrical geometry. Our approach is to model the plasma phase in the absence of dust particles using the local field drift-diffusion model based on which a description of the electrons and ions kinetics in conjunction with the electric potential is obtained. Then, using these plasma variables, we carry out a separate simulation of the particles charging and motion. The primary focus of this study in the particle phase is the structures formed by a few interacting particles injected into the plasma from the upper electrode, after the glow discharge reaches its quasisteady-state (for a detailed analysis on the temporal behavior of such particles, refer to Refs. [29,31].) Each of these particles, along with their accumulated charge, is tracked through the bulk and sheath in a three-dimensional Lagrangian framework. Molecular dynamics and particle simulation of dust structures without modeling the plasma phase have been conducted by Hammerberg *et al.* [32] and Joyce *et al.* [33], respectively. Including the gas flow, Kim an Manousiouthakis [34] simulated transport of noninteracting particles in a rf parallel plate reactor. The only comprehensive numerical investigation of the entire coupled phenomenon, to the best of the authors knowledge, is that by Vyas and Kushner [23]. Apart from dissimilarities involved in the geometry and modeling of the plasma phase, major differences of our work with this study lie in the proposed model for ion streaming effect, examination of two-dimensional (2D) Coulomb crystals in the limit of a small number of particles, and results pertaining to the bilayer configuration of the particles.

In the following section we present the plasma model used in this study. Equations for dust particles together with various forces acting on them and the ion focus model are explained in Sec. III. The results of the simulations are presented and discussed in Sec. IV. Finally, some concluding remarks are provided in Sec. V.

II. PLASMA MODEL

We consider a cylindrical rf glow discharge plasma reactor, with interelectrode gap H and electrodes radii R, as shown in Fig. 1. The local field approximation model consists of the following set of equations [35]:

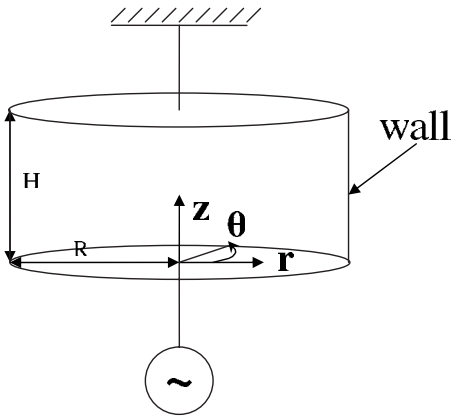

FIG. 1. Schematic of the problem.

$$\frac{\partial n_{e,i}}{\partial t} + \vec{\nabla} \cdot \vec{\Gamma}_{e,i} = G_{e,i} - L_{e,i}, \tag{1}$$

$$\nabla^2 \phi = \frac{e}{\epsilon_0}(n_e - n_i), \tag{2}$$

where

$$\vec{\Gamma}_e = -n_e \mu_e \vec{E} - D_e \vec{\nabla} n_e, \tag{3}$$

$$\vec{\Gamma}_i = +n_i \mu_i \vec{E} - D_i \vec{\nabla} n_i, \tag{4}$$

$$\vec{E} = -\vec{\nabla}\phi, \tag{5}$$

$$G_{e,i} = \alpha |\vec{\Gamma}_e|, \tag{6}$$

$$L_{e,i} = \beta n_e n_i. \tag{7}$$

In the above set of equations, $n_{e,i}$ refers to electron, ion number density, and $\vec{\Gamma}_{e,i}$ denotes electron, ion flux. $G_{e,i}$ is the electron, ion generating source term, while $L_{e,i}$ designates electron, ion rate of loss. The electric potential is represented by ϕ and the electric field by $\vec{E}$. The elementary charge is shown by e, and $\mu_{e,i}$ and $D_{e,i}$ represent electron, ion mobility and diffusion coefficients, respectively. Finally, α and β are Townsend coefficients for ionization and recombination. Equations (1), (3), and (4) form a set of two convection-diffusion transport equations, while Eq. (5) couples them to the Poisson's equation (2) for electric potential. Equations (6) and (7) represent, respectively, forms of the source and loss terms in the first equation. Denoting the unit vectors corresponding to the r, z, and θ directions in the cylindrical coordinate system by $\hat{e}_r$, $\hat{e}_z$, and $\hat{e}_\theta$, respectively, yields

$$\vec{\nabla} \equiv \frac{\partial}{\partial r}\hat{e}_r + \frac{1}{r}\frac{\partial}{\partial \theta}\hat{e}_\theta + \frac{\partial}{\partial z}\hat{e}_z,$$

$$\vec{\nabla}\cdot\vec{\Gamma} \equiv \frac{1}{r}\frac{\partial(r\Gamma_r)}{\partial r} + \frac{1}{r}\frac{\partial\Gamma_\theta}{\partial\theta} + \frac{\partial\Gamma_z}{\partial z},$$

$$\nabla^2\phi \equiv \frac{1}{r}\frac{\partial}{\partial r}\left(r\frac{\partial\phi}{\partial r}\right) + \frac{1}{r^2}\frac{\partial^2\phi}{\partial\theta^2} + \frac{\partial^2\phi}{\partial z^2}.$$

As the geometry under consideration suggests, there is symmetry around the axis (corresponding to $r=0$). Thus variables do not vary with θ, all the terms containing $\partial/\partial\theta$ can be dropped, and the problem is reduced to that of an axisymmetic one. We make use of this feature and for the plasma phase, restrict our computational domain to only the plane surrounded by the electrodes on top and bottom ($0 \leqslant z \leqslant H$), the wall on the right and the axis of symmetry on the left ($0 \leqslant r \leqslant R$).

On the reactor axis the boundary condition for any variable $\xi = n_e$, n_i, and ϕ satisfies the symmetry condition,

$$\left.\frac{\partial\xi}{\partial r}\right|_{r=0} = 0. \tag{8}$$

Inside the sheaths, close to the electrodes or reactor wall where the largest electric field is expected, the diffusion term $(-D\vec{\nabla}n)$ in the particles flux expression is negligible comparing to the drift term $(\pm n\mu\vec{E})$ caused by the electric field. Hence the gradients of plasma particles number densities are set to zero in the incoming flux towards the boundaries. Furthermore, since there is no ion detachment from the electrodes or wall, total ions outgoing normal flux from the electrodes or wall towards the bulk plasma is set to zero,

$$\vec{\Gamma}_i\cdot\hat{n} = \begin{cases} +n_i\mu_i\vec{E}\cdot\hat{n}, & \vec{E}\cdot\hat{n} \geqslant 0, \\ 0, & \vec{E}\cdot\hat{n} < 0, \end{cases} \tag{9}$$

where $\hat{n}$ represents the unit vector perpendicular to the boundary surface and directed towards the electrodes or wall of the reactor. The electrodes are assumed to be perfectly absorbing and no secondary electrons are emitted off them. Thus similarly,

$$\vec{\Gamma}_e\cdot\hat{n} = \begin{cases} 0, & \vec{E}\cdot\hat{n} \geqslant 0, \\ -n_e\mu_e\vec{E}\cdot\hat{n}, & \vec{E}\cdot\hat{n} < 0. \end{cases} \tag{10}$$

On the surface of the reactor wall the only incoming (with respect to the electrode) electrons are the thermalized ones with the mean thermal velocity $v_{th_e} = \sqrt{8k_BT_e/\pi m_e}$, where m_e designates electron mass. Meanwhile, as a source of the outgoing electrons, we consider the secondary electron emission phenomenon which arises from ions impact on the wall. Therefore electrons outgoing normal drift flux is proportional to the ions incoming normal drift flux, with γ (the secondary electron emission coefficient) being the proportionality factor,

$$-n_e\mu_e\vec{E}\cdot\hat{n} = \begin{cases} -\gamma n_i\mu_i\vec{E}\cdot\hat{n}, & \vec{E}\cdot\hat{n} \geqslant 0, \\ \frac{1}{4}n_e v_{th_e}, & \vec{E}\cdot\hat{n} < 0. \end{cases} \tag{11}$$

As boundary conditions for the electric potential, the upper electrode is grounded, and the lower electrode is powered by a periodic voltage with magnitude ϕ_{rf} and frequency f. The external circuit is not considered and no dc bias voltage is applied to the electrodes. Therefore

$$\phi(z=0) = \phi_{rf}\cos(2\pi ft), \tag{12}$$

$$\phi(z=H) = 0. \tag{13}$$

The charge density distribution along the dielectric wall, σ, is found by temporally integrating the summation of electrons $(\vec{J}_e)$ and ions $(\vec{J}_i)$ normal current densities at each node on the wall [36,37],

$$\frac{\partial\sigma}{\partial t} = \vec{J}_e\cdot\hat{n} + \vec{J}_i\cdot\hat{n}, \tag{14}$$

with $\vec{J}_e = -e\vec{\Gamma}_e$, and $\vec{J}_i = +e\vec{\Gamma}_i$. Then, the normal electric field is imposed on the surrounding wall according to Gauss's law [36,37],

$$-\vec{E}\cdot\hat{n} = \frac{\sigma}{\epsilon_0}. \tag{15}$$

Note that the normal electric field will be nonuniform along the dielectric wall. Moreover, we are assuming the insulator wall of the cylinder to be a surface (with no thickness). For the case where the radial wall has a finite thickness, the above relation should be modified to incorporate the effect of the normal electric field (due to the polarization of dielectric material) at the interface from the wall side. Hence the Poisson equation needs to be solved within the wall too. This case is beyond the scope of the present study.

There exist singular points on the circle where the electrodes are attached to the chamber wall. To circumvent this singularity problem we linearize the potential along the electrodes from its value on the wall to its magnitude on the electrodes within a distance of 5% of the radius from the singular points. It is worth mentioning that this is a more natural technique than linearization of the potential on the wall where the value of the normal electric field (and not the potential itself) is imposed.

The numerical scheme together with the nonuniform staggered-grid mesh stencil employed to solve the above set of equations and boundary conditions is elaborated for the one-dimensional case elsewhere [29]. We used a semi-implicit forward Euler method for temporal integration of ions and electrons "fluid" equations in which the convective and diffusive fluxes are discretized using the upwind and central difference, respectively. This leads to a system of coupled algebraic equations for the discrete variables. At each time step, these coupled equations are solved iteratively until a reasonable convergence of the variables is reached. Inside each internal iteration, a Gauss-Seidel method is employed to solve each of the equations.

III. PARTICLES EQUATIONS AND THE MODEL

Tracking a swarm of spherical dust particles (which could be of different masses and radii) is possible in Lagrangian

framework. It should be stressed that due to the low particle loading, we assume that the presence of dust particles does not significantly alter the plasma structure. As a result, our approach does not account for the electron depletion or any other effects of the dust particles on the discharge balance. Moreover, since the dust particles are much heavier than the plasma species, they do not respond to the fast varying plasma properties in one rf period. Therefore after the temporal and spatial variations of plasma variables are resolved via the plasma model simulation, they are averaged over the rf period, and the resultant averaged potential, densities, and velocities are fed as inputs into the particle simulation module to compute the charge and forces on the particles. In addition to the particles equations of motion, we account for the charging process of the particles by solving the transient charging equation. The Lagrangian vectorial equations for the mth particle position, velocity, and charge are described, respectively, as

$$\frac{d\vec{x}_p^m}{dt} = \vec{v}_p^m, \tag{16}$$

$$\frac{d\vec{v}_p^m}{dt} = \frac{\vec{F}_t^m}{m_p^m}, \tag{17}$$

$$\frac{dQ_p^m}{dt} = I_e^m + I_i^m. \tag{18}$$

Here, $\vec{F}_t^m$ is the total force acting on the mth particle, and $m_p^m = 4\pi\rho_p^m (a_p^m)^3/3$ the mth particle mass with ρ_p^m its mass density. I_e^m and I_i^m indicate, respectively, electron and ion currents towards the mth particle. In the present analysis where we simulate the discharge in a cylindrical geometry, the above equations are accounted for in r, z, and θ directions. (Note that although the plasma field is axisymmetric, particle motion is three-dimensional due to interaction with other particles.) In the noninertial cylindrical coordinates (see Fig. 1), the left-hand side of Eq. (17) can be rewritten as

$$\frac{d\vec{v}_p^m}{dt} = \frac{d}{dt}(v_{p_\theta}^m \hat{e}_\theta + v_{p_r}^m \hat{e}_r + v_{p_z}^m \hat{e}_z)$$

$$= \frac{dv_{p_\theta}^m}{dt}\hat{e}_\theta + v_{p_\theta}^m \frac{d\hat{e}_\theta}{dt} + \frac{dv_{p_r}^m}{dt}\hat{e}_r + v_{p_r}^m \frac{d\hat{e}_r}{dt} + \frac{dv_{p_z}^m}{dt}\hat{e}_z.$$

With $\omega_p^m = v_{p_\theta}^m / r^m$, the rotational angular velocity of the unit vectors with respect to the inertial Cartesian reference system having the same origin, time derivative of the unit vectors are

$$\frac{d\hat{e}_\theta}{dt} = -\omega_p^m \hat{e}_r = -\frac{v_{p_\theta}^m}{r^m}\hat{e}_r, \quad \frac{d\hat{e}_r}{dt} = \omega_p^m \hat{e}_\theta = \frac{v_{p_\theta}^m}{r^m}\hat{e}_r.$$

Therefore in the cylindrical coordinate system the complete set of scalar equations for the mth particle motion, which incorporates Coriolis effect and centrifugal force [38], becomes

$$\frac{d\theta_p^m}{dt} = \frac{v_{p_\theta}^m}{r^m},$$

$$\frac{dr_p^m}{dt} = v_{p_r}^m,$$

$$\frac{dz_p^m}{dt} = v_{p_z}^m,$$

$$\frac{dv_{p_\theta}^m}{dt} = \frac{F_{t_\theta}^m}{m_p^m} - \frac{v_{p_\theta} v_{p_r}}{r^m},$$

$$\frac{dv_{p_r}^m}{dt} = \frac{F_{t_r}^m}{m_p^m} + \frac{v_{p_\theta}^2}{r^m},$$

$$\frac{dv_{p_z}^m}{dt} = \frac{F_{t_z}^m}{m_p^m}. \tag{19}$$

These equations are integrated using the second order Adams-Bashforth method with specified initial conditions.

The main forces on the dust particles in a discharge comprise the electric (denoted by $\vec{F}_e^m$), gravitational ($\vec{F}_g^m = -m_p^m g \hat{e}_z$, where g is the gravitational constant), ion drag ($\vec{F}_{id}^m$), neutral drag ($\vec{F}_{nd}^m$), and particle-particle interaction ($\vec{F}_{mn}^m$) forces. In the present work, we assume that no temperature gradient is present in the discharge, hence no thermophoretic force is acting on the particles. (An analysis of the effect of this force on the particle dynamics is performed in Ref. [39].) Therefore $\vec{F}_t^m = \vec{F}_e^m + \vec{F}_g^m + \vec{F}_{id}^m + \vec{F}_{nd}^m + \vec{F}_{mn}^m$.

It is crucial to monitor the interparticle distances especially in the particles final structure to ensure that the surrounding plasma potential is not disrupted due to the particles mutual shielding (i.e., the particles potential interference, not the plasma ions streaming phenomenon) [40]. The condition that for each particle m, the so-called lattice parameter $k > 1$ implies that use of the following orbital motion limited (OML) expressions [41] (with a range of applicability $a_p^m \ll \lambda_D$) to determine the currents in Eq. (18) as well as the ion drag model remains as robust as in the case of an isolated particle:

$$I_e^m = -en_e \pi (a_p^m)^2 v_{th_e} \exp\left[\frac{e(\phi_p^m - \phi^m)}{k_B T_e}\right], \tag{20}$$

$$I_i^m = en_i \pi (a_p^m)^2 v_s^m \left[1 - \frac{2e(\phi_p^m - \phi^m)}{m_i (v_s^m)^2}\right], \tag{21}$$

$$Q_p^m = 4\pi\epsilon_0 a_p^m (\phi_p^m - \phi^m). \tag{22}$$

Here, ϕ_p^m is the mth particle surface potential and $v_s^m = \sqrt{v_{th_i}^2 + (v_{ip}^m)^2}$ is the ion mean speed with which ions approach the mth dust particle. In the latter relation, $v_{th_i} = \sqrt{8k_B T_i/\pi m_i}$ is the mean ion thermal velocity and $\vec{v}_{ip}^m = \vec{v}_i^m - \vec{v}_p^m$ is the ion velocity relative to the mth particle (with ion

velocity obtained from $\vec{v}_i=\vec{\Gamma}_i/n_i$). T_i and m_i indicate ion temperature and mass, respectively. It is emphasized that the effect of the degree of collisionality of the plasma (enhanced by ion-neutral charge-exchange collisions) on the ion current [30,42,43] and the ion drag force is not included in this work. From Eqs. (18) and (20)–(22), the potential difference between the mth particle and the surrounding plasma, i.e., the floating potential ($\phi_p^m-\phi^m$), and the mth particle charge, Q_p^m, can be evaluated at each time step. With the knowledge of the plasma electric field at the particle location and the amount of charge accumulated on the particle, the electric force on the mth particle is simply obtained from [44,45]

$$\vec{F}_e^m = Q_p^m \vec{E}\left[1+\frac{\left(\frac{a_p^m}{\lambda_D^m}\right)^2}{3\left(1+\frac{a_p^m}{\lambda_D^m}\right)}\right]. \tag{23}$$

$\lambda_D^m=\{e^2 n_e^m/\epsilon_0 k_B T_e+e^2 n_i^m/[\epsilon_0 k_B T_i+m_i(v_{ip}^m)^2]\}^{-1/2}$ defines the effective (linearized) Debye length at the location of the mth particle. In our case, $a_p^m \ll \lambda_D^m$, and the effect of the last term which represents the enhancement in the surface field of macroscopic bodies (as opposed to point charges) vanishes. Nevertheless, we keep this term in our formulation for the sake of completeness.

Despite its significant role in dusty plasmas, a self-consistent model for the ion drag force (especially in collisional regime) has yet not been presented. In our recent work [29], we compared and contrasted two of the well-known models by Barnes *et al.* [41] and Khrapak *et al.* [46], and concluded that for the parameters under study adopting the standard approach of Barnes *et al.* with electron Debye length would more closely agree with the results observed in the experiments [47,48]. Here, we use the model of Barnes *et al.* [41],

$$\vec{F}_{id}^m = \pi n_i^m v_s^m m_i \vec{v}_{ip}^m (b_c^m)^2 + 4\pi n_i^m v_s^m m_i \vec{v}_{ip}^m (b_{\pi/2}^m)^2 \ln \Gamma^m, \tag{24}$$

where the collection impact parameter is defined as

$$b_c^m = a_p^m\left[1-\frac{2e(\phi_p^m-\phi)}{m_i(v_s^m)^2}\right]^{1/2}. \tag{25}$$

Moreover, we have found in our previous simulations that the inclusion of ions thermal energy (refer to the definition of v_s) in the calculation of the above collection impact parameter is vital in capturing the physics of particle dynamics. Also,

$$b_{\pi/2}^m = \frac{e(\phi_p^m-\phi)}{m_i(v_s^m)^2} \tag{26}$$

is the orbital impact parameter corresponding to a 90° deflection, and

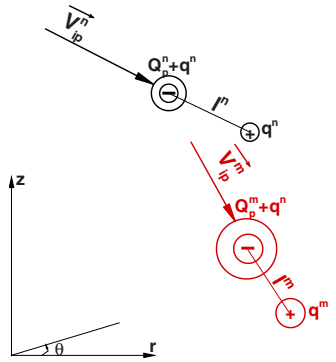

FIG. 2. (Color online) Schematic of the proposed model of ion focus effect.

$$\ln \Gamma^m = \frac{1}{2}\ln\left[\frac{(\lambda_{D_e}^m)^2+(b_{\pi/2}^m)^2}{(b_c^m)^2+(b_{\pi/2}^m)^2}\right] \tag{27}$$

is the Coulomb logarithm, where $\lambda_{D_e}^m=\sqrt{\epsilon_0 k_B T_e/e^2 n_e}$ describes the electron Debye length at the location of the mth particle.

While considering no gas flow, i.e., $\vec{v}_n^m=0$, we assume a specular reflection of the neutral particles after their collision with the particle, and utilize the following Epstein expression for calculation of the neutral drag force [49]:

$$\vec{F}_{nd}^m = \frac{8}{3}\sqrt{2\pi}(a_p^m)^2 m_n n_n v_{th_n}(\vec{v}_n^m-\vec{v}_p^m). \tag{28}$$

Assuming thermal equilibrium between ions and neutral species, $T_n=T_i$, $n_n=P/k_B T_i$ gives the neutral number density, with P denoting the reactor pressure. $v_{th_n}=\sqrt{k_B T_i/m_n}$ is the thermal velocity of neutral species with mass $m_n \simeq m_i$.

Particle-particle interaction model

In the regions where the spherical symmetry of the particle sheath remains essentially intact (e.g., central part of the discharge) the Debye-Huckel (Yukawa) potential adequately describes the sheath around the particle [45]. This isotropy condition is satisfied in the regime of subthermal ion flow if the interparticle distances are greater than the local effective Debye length. Approaching the sheath, however, the drift velocity of the ions increasingly exceeds their thermal velocity which results in the anisotropy of the plasma through the ion wake phenomenon downstream of the particle. As a result, dust particles at different vertical positions indeed may interact by net attractive forces [9–11,21,22,50,51].

As mentioned previously, strong ion flow causes deformation (i.e., dielectric polarization) of the sheath around the particle. Following Yaroshenko *et al.* [24], we model this ion focusing effect by introducing a positive pointlike charge q^m located within the Debye sphere at a distance l^m downstream of the particle ($\vec{l}^m=l^m\vec{v}_{ip}^m/v_{ip}^m$). Accordingly, as shown in Fig. 2, the system of a charged particle with its ion density enhancement is considered as a superposition of the uncompensated residual plasma shielded monopole $Q_p^m+q^m$, plus a plasma shielded electric dipole $\vec{P}^m=q^m\vec{l}^m$, where

$$q^m = f_q^m |Q_p^m|, \quad l^m = f_l^m \lambda_D^m. \tag{29}$$

f_q^m and f_l^m are the empirical parameters of the model. Their accurate description calls for elaborate experiments and numerical simulations which can quantify their relation to the various parameters involved such as pressure (degree of collisionality), local ion velocity, etc. Schweigert *et al.* [18] have presented Monte Carlo calculations of the ion motion through a two-layer dust crystal located in the electrode sheath of a rf discharge. In their analysis, formation of a region of enhanced ion density (ion cloud) by focused ions is confirmed and modeled through replacing each ion cloud by a positive point charge located below the upper particle. Then, the model parameters, i.e., q and l, are obtained via a curve-fit of their model to the simulation results. From their findings it can be concluded that the more negative the charge on the particle is the more pronounced the ion focus effective charge will be, and the closer to the particle it will be focused. We incorporate this effect of the particles charge into the expressions for f_q^m and f_l^m as follows:

$$f_q^m = f \frac{Q_p^m}{\max(|Q_p^m|, |Q_p^n|)}, \quad f_l^m = f' \frac{\max(|Q_p^m|, |Q_p^n|)}{Q_p^m}. \tag{30}$$

We note that on conductive particles, dipole moments, which in a simple approximation relate to a_p^3, may be induced by the local electric field [52–54]. Moreover, the asymmetry of charge distribution between the leading and trailing hemispheres of dielectric particles in a flowing plasma leads to a nonuniform surface potential which can be represented accurately using a dipole whose strength is proportional to a_p^2 [54–56]. In either case, the resulting interparticle interactions are shown to be insignificant for small particles such as those of this study [54]. Nonetheless, adopting the appropriate expressions for the corresponding dipoles, the following formulation can be employed for these cases as well.

Taking the electrostatic screened potential around the monopole of the nth particle as the Debye-Huckel form,

$$\phi_n^M = \frac{Q_p^n + q^n}{4\pi\epsilon_0 |\vec{r} - \vec{r}_n|} \exp\left(- \frac{|\vec{r} - \vec{r}_n|}{\lambda_D^n} \right), \tag{31}$$

one can readily calculate the repulsive screened Coulomb force on the monopole m exerted by the monopole n in the following manner:

$$\vec{F}_{mn}^{MM} = -(Q_p^m + q^m) \left. \frac{\partial \phi_n^M}{\partial \vec{r}} \right|_{\vec{r}=\vec{r}_m} = \frac{(Q_p^n + q^n)(Q_p^m + q^m)}{4\pi\epsilon_0 |\vec{r}_m - \vec{r}_n|^2} \times \exp\left(- \frac{|\vec{r}_m - \vec{r}_n|}{\lambda_D^n} \right) \left[1 + \frac{|\vec{r}_m - \vec{r}_n|}{\lambda_D^n} \right] \frac{\vec{r}_m - \vec{r}_n}{|\vec{r}_m - \vec{r}_n|}. \tag{32}$$

The use of local Debye radius means the interaction is mediated by the surrounding plasma and may not be equally reciprocal for particles at different regions with dissimilar plasma properties. It can also explain some of the experimental observations made by Hebner and Riley [22].

The plasma shielded potential around the dipole n can be written as [53]

$$\phi_n^D = \frac{\vec{P}^n \cdot (\vec{r} - \vec{r}_n - 0.5\vec{l}_n)}{4\pi\epsilon_0 |\vec{r} - \vec{r}_n - 0.5\vec{l}_n|^3} \left[1 + \frac{|\vec{r} - \vec{r}_n - 0.5\vec{l}_n|}{\lambda_D^n} \right] \times \exp\left(- \frac{|\vec{r} - \vec{r}_n - 0.5\vec{l}_n|}{\lambda_D^n} \right). \tag{33}$$

Therefore the dipole-dipole interaction force exerted on the dipole m by the dipole n is [57]

$$\vec{F}_{mn}^{DD} = \left. \frac{\partial}{\partial \vec{r}} \left(- \frac{\partial \phi_n^D}{\partial \vec{r}} \cdot \vec{P}^m \right) \right|_{\vec{r}=\vec{r}_m + 0.5\vec{l}_m} = \frac{1}{4\pi\epsilon_0 |\vec{r}_m + 0.5\vec{l}_m - \vec{r}_n - 0.5\vec{l}_n|^6} \exp\left(- \frac{|\vec{r}_m + 0.5\vec{l}_m - \vec{r}_n - 0.5\vec{l}_n|}{\lambda_D^n} \right) \left\{ \left[3|\vec{r}_m + 0.5\vec{l}_m - \vec{r}_n - 0.5\vec{l}_n| + 3\frac{|\vec{r}_m + 0.5\vec{l}_m - \vec{r}_n - 0.5\vec{l}_n|^2}{\lambda_D^n} + \frac{|\vec{r}_m + 0.5\vec{l}_m - \vec{r}_n - 0.5\vec{l}_n|^3}{\lambda_D^{n^2}} \right] [\vec{P}^m \cdot \vec{P}^n (\vec{r}_m + 0.5\vec{l}_m - \vec{r}_n - 0.5\vec{l}_n) + \vec{P}^n \cdot (\vec{r}_m + 0.5\vec{l}_m - \vec{r}_n - 0.5\vec{l}_n) \vec{P}^m + \vec{P}^m \cdot (\vec{r}_m + 0.5\vec{l}_m - \vec{r}_n - 0.5\vec{l}_n) \vec{P}^n] - \left[\frac{15}{\lambda_D^n} + \frac{15}{|\vec{r}_m + 0.5\vec{l}_m - \vec{r}_n - 0.5\vec{l}_n|} + \frac{6|\vec{r}_m + 0.5\vec{l}_m - \vec{r}_n - 0.5\vec{l}_n|}{\lambda_D^{n^2}} + \frac{|\vec{r}_m + 0.5\vec{l}_m - \vec{r}_n - 0.5\vec{l}_n|^2}{\lambda_D^{n^3}} \right] \vec{P}^m \cdot (\vec{r}_m + 0.5\vec{l}_m - \vec{r}_n - 0.5\vec{l}_n) \vec{P}^n \cdot (\vec{r}_m + 0.5\vec{l}_m - \vec{r}_n - 0.5\vec{l}_n) (\vec{r}_m + 0.5\vec{l}_m - \vec{r}_n - 0.5\vec{l}_n) \right\}. \tag{34}$$

It should be noted that the distances are calculated from/to the center of the dipole. In the vacuum limit, i.e., $\lambda_D^n \to \infty$, the component of this force along $(\vec{r}_m - \vec{r}_n)$, when assuming $\vec{P}^m = \vec{P}^n$ and that ions flow in the vertical direction, reduces to the corresponding expression in Ref. [24]. Meanwhile, the potential energy calculated from the above plasma shielded interaction force simplifies to Eq. (12) of Ref. [52], if both of the particles have the same dipole moment.

The force on the dipole m applied by the electric field of the monopole n is derived as

$$\vec{F}_{mn}^{DM} = \frac{\partial}{\partial \vec{r}}\left(-\frac{\partial \phi_n^M}{\partial \vec{r}}\cdot \vec{P}^m\right)\Bigg|_{\vec{r}=\vec{r}_m+0.5\vec{l}_m} = \frac{(Q_p^n+q^n)}{4\pi\epsilon_0|\vec{r}_m+0.5\vec{l}_m-\vec{r}_n|^3}\exp\left(-\frac{|\vec{r}_m+0.5\vec{l}_m-\vec{r}_n|}{\lambda_D^n}\right)$$
$$\times\left\{\left[1+\frac{|\vec{r}_m+0.5\vec{l}_m-\vec{r}_n|}{\lambda_D^n}\right]\vec{P}^m-\left[3+3\frac{|\vec{r}_m+0.5\vec{l}_m-\vec{r}_n|}{\lambda_D^n}+\frac{|\vec{r}_m+0.5\vec{l}_m-\vec{r}_n|^2}{\lambda_D^{n^2}}\right]\vec{P}^m\cdot\frac{(\vec{r}_m+0.5\vec{l}_m-\vec{r}_n)}{|\vec{r}_m+0.5\vec{l}_m-\vec{r}_n|}\frac{(\vec{r}_m+0.5\vec{l}_m-\vec{r}_n)}{|\vec{r}_m+0.5\vec{l}_m-\vec{r}_n|}\right\}. \quad (35)$$

Finally, the force on the monopole m applied by the electric field of the dipole n can be rendered as

$$\vec{F}_{mn}^{MD} = -(Q_p^m+q^m)\left.\frac{\partial \phi_n^D}{\partial \vec{r}}\right|_{\vec{r}=\vec{r}_m} = -\frac{(Q_p^m+q^m)}{4\pi\epsilon_0|\vec{r}_m-\vec{r}_n-0.5\vec{l}_n|^3}\exp\left(-\frac{|\vec{r}_m-\vec{r}_n-0.5\vec{l}_n|}{\lambda_D^n}\right)$$
$$\times\left\{\left[1+\frac{|\vec{r}_m-\vec{r}_n-0.5\vec{l}_n|}{\lambda_D^n}\right]\vec{P}^n-\left[3+3\frac{|\vec{r}_m-\vec{r}_n-0.5\vec{l}_n|}{\lambda_D^n}+\frac{|\vec{r}_m-\vec{r}_n-0.5\vec{l}_n|^2}{\lambda_D^{n^2}}\right]\vec{P}^n\cdot\frac{(\vec{r}_m-\vec{r}_n-0.5\vec{l}_n)}{|\vec{r}_m-\vec{r}_n-0.5\vec{l}_n|}\frac{(\vec{r}_m-\vec{r}_n-0.5\vec{l}_n)}{|\vec{r}_m-\vec{r}_n-0.5\vec{l}_n|}\right\}. \quad (36)$$

With the assumption of $Q_p^m=Q_p^n$ and $\vec{P}^m=\vec{P}^n$, $\vec{F}_{mn}^{DM}$ and $\vec{F}_{mn}^{MD}$ cancel each other, as also mentioned in Ref. [52].

In order to track each particle in the computational domain and find its host computational cell, we employ an efficient generalized iterative algorithm for searching and locating particles in arbitrary meshes [58]. The algorithm uses Newton's method to search for the particle within a reference element mapped from the quadrilateral computational mesh elements, together with a criterion to efficiently move from element to element in the mesh. To calculate the forces and particle charge, at each time step, all time-averaged (over the rf period) plasma variable related terms have to be calculated at the particle instantaneous position. This is performed by interpolation of the corresponding time-averaged plasma variables present in the above expressions from the host element grid points to the particle location using a two-point Lagrange interpolation in r and z directions.

IV. RESULTS AND DISCUSSION

A. Validation of the code

Imposing a gradient-free condition on all the variables along the left and right boundaries, we conducted a validation study by solving the *planar* 2D equations for both plasma phase and one single particle within a rectangle of length $L=1$ cm and height $H=2$ cm. In such a case, it is trivial to analytically show that Eqs. (1)–(7) will give the same results as the 1D (varying along only the y direction) case. Figure 3(a) depicts time-averaged (over one rf period) profiles of concentrations of plasma particles and electric field along the y direction in the reactor. Plotted in Fig. 3(b) is the time history of the position of a single particle with $a_p=1.0$ μm and $\rho_p=2000$ kg/m^3, initially released from the top electrode ($y=H$). As expected, the results of the present 2D planar case coincide with those from the previous 1D

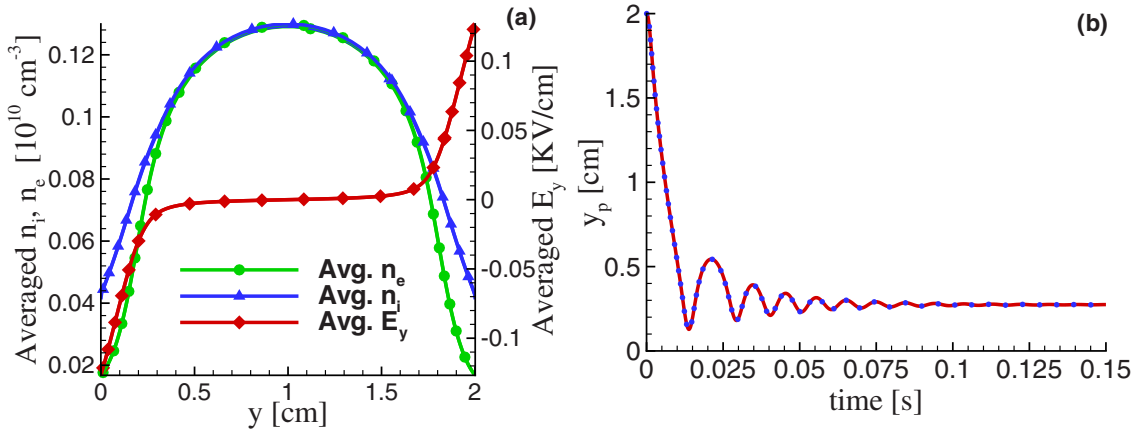

FIG. 3. (Color online) Validation of the code. (a) Time-averaged (over one rf period) electrons and ions densities, and electric field along the y direction in the discharge, (b) temporal variation of vertical position for one single particle with $a_p=1.0$ μm and $\rho_p=2000$ kg/m^3 released from the top electrode. Lines show the results from the present 2D planar case. Symbols show the results from the previous 1D case [29].

TABLE I. Parameters used in the simulation of plasma phase.

Parameter	Value
$\mu_e P$	$3\times10^5\left(\frac{\text{cm}^2}{\text{V s}}\text{torr}\right)$
D_e	$\frac{\mu_e k_B T_e}{e}\left(\frac{\text{cm}^2}{\text{s}}\right)$
$\mu_i P$	$1.4\times10^3\left(\frac{\text{cm}^2}{\text{V s}}\text{torr}\right)$
$D_i P$	$40\left(\frac{\text{cm}^2}{\text{s}}\text{torr}\right)$
α/P	$29.22\exp\left[-26.64\times\left(\frac{P}{E}\right)^{1/2}\right]\left(\frac{1}{\text{cm}}\right)$
β	$0\left(\frac{\text{cm}^3}{\text{s}}\right)$
f	13.56 (MHz)
H	2 (cm)
R	1 (cm)
P	200 (mtorr)
T_e	4 (eV)
$T_i=T_n$	300 (K)
γ	0.05
ϕ_{rf}	40 (V)

case in Ref. [29]. Noteworthy is that in the 2D code, we tested the cases with nonuniform initial conditions for plasma variables, and also cases where the particle was released at a position away from $x=0$. The former ended with the same results as starting with a uniform spatial distribution of plasma variables. The latter yielded an identical trajectory compared to the one where the particle is released at $x=0$.

B. Plasma phase

The values of transport coefficients and various parameters of the argon discharge used in the simulation are tabulated in Table I. After a resolution study, we decided to use a nonuniform grid in both r and z directions with 60×60 grid points and finer grid-spacing close to the electrodes and wall. Figures 4(a)–4(e) depict, respectively, averaged (over time) profiles of concentrations of ions, electrons, electric field in r and z directions, and electric potential in the reactor. The structure of the contours of plasma particles densities is almost circular. From the figure it is evident that plasma sheaths form not only in the vicinity of electrodes, but also in the region adjacent to the surrounding wall. Naturally, within the sheaths of the electrodes the magnitude of the electric field in the z direction is large and the electric field in the r direction is not noticeable. This trend is reversed inside the sheath of the radial wall. Further, the averaged ion r and z velocities are in the direction of the averaged electric fields in the corresponding directions. One can conclude that, in the average sense, the ions flow towards the electrodes and the radial wall. Another interesting feature (repeatedly observed in the discharge experiments) captured by the physical wall boundary conditions used in this simulation is the negative averaged electric potential along the radial wall with a value of ~-3.7 V in the central regions of the wall [see Figs. 4(e) and 4(f)].

C. Particles

Here, we choose melamine formaldehyde particles with $\rho_p=1514\ \text{kg/m}^3$. As initial conditions for Eqs. (16)–(18), particles are placed on a ring with radius 0.1 cm at the top electrode, with zero charge and velocity. Following the experimental procedure by Thomas *et al.* [1], particles with $a_p=1.0\ \mu$m are injected one by one, each after the system attains equilibrium (which typically happens after 1 s). We emphasize that we do not seek any quantitative agreement (e.g., interparticle distances) between our results and those of the experiment as we did not exactly simulate the operating parameters and electrode and wall configurations of the experiment. For monodisperse particles forming monolayer structures, in order to retain the physics of ion focus phenomenon consistently, we include all the interactions by choosing $f=f'=0.65$. Nevertheless, similar, but more expanded (due to larger charges of monopoles), configurations would be obtained when including only the screened Coulomb force, i.e., setting $f=f'=0$.

Without including the particles interaction, all of the particles would become trapped at the same location which corresponds to the potential energy well of the reactor (located on the reactor axis and in the lower electrode sheath) [31]. With interparticle interactions included, various multishell structures formed by the particles in the horizontal (X-Y) plane at the end of their motion are depicted in Fig. 5 and compared to the experimental results of Thomas *et al.* [1]. Noting the very likely differences in the angles of view from the top (or choice of $\theta=0$ line) and thus excluding the rigid body rotation of the whole structures, excellent qualitative agreement is seen. In the course of the particles transport and trapping, particle-particle interaction becomes significant in the regions where their spacing becomes of the order of the local plasma Debye length (mostly in the last part of their motion while becoming trapped in the sheath). It is this interaction in conjunction with the shape of the potential energy curve near its well that dictates the morphology of the assemblies which particles form at the end of their motions. The geometrically symmetric feature of the problem might

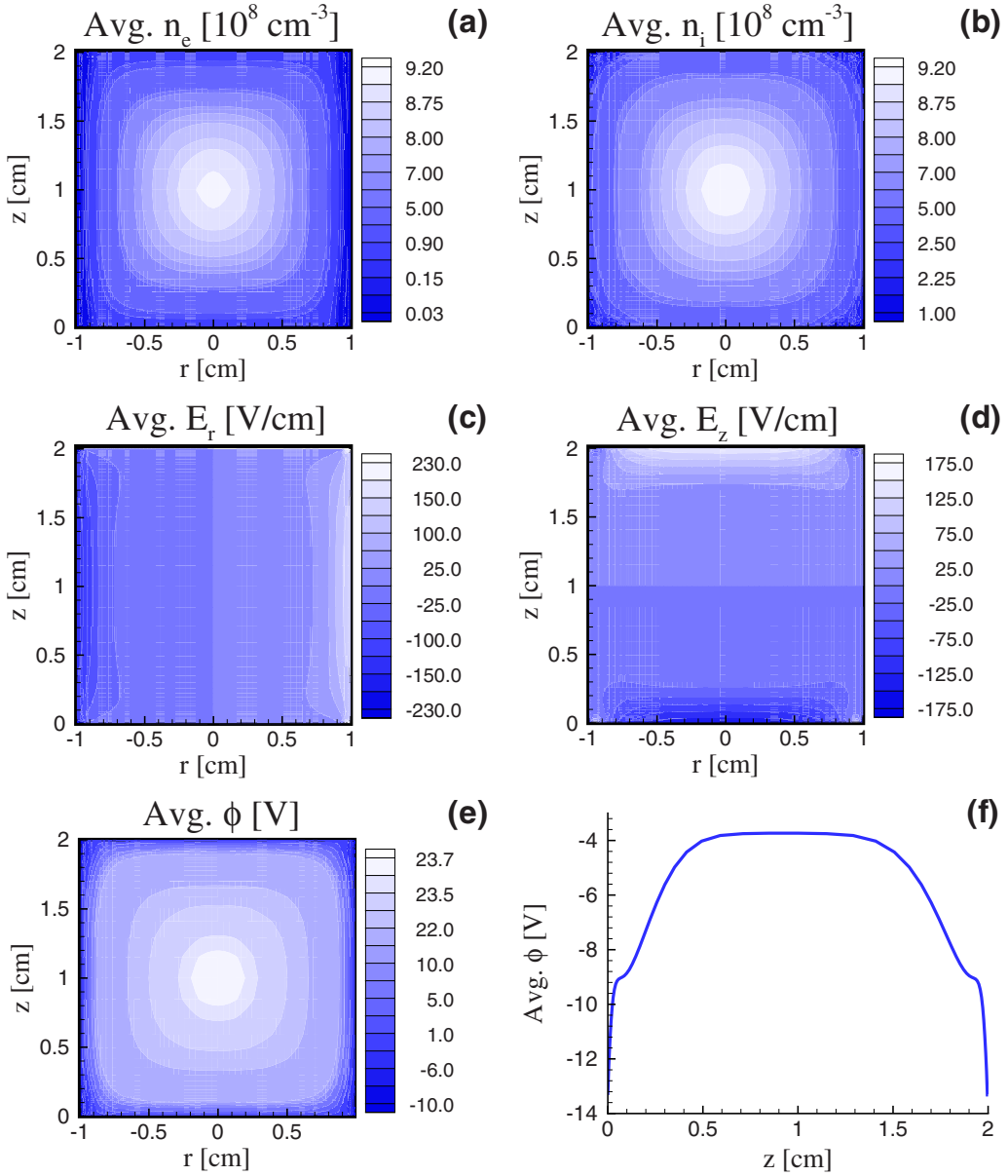

FIG. 4. (Color online) Spatial distribution of time-averaged (a) electrons, and (b) ions concentrations, and electric field in the (c) r, (d) z directions, electric potential (e) within the reactor and (f) along the wall of the reactor, for the operating conditions of Table I.

erroneously suggest that at their equilibrium, particles should distribute on a ring. We stress that such an unstable equilibrium configuration was indeed observed in our simulations when the particles were released all together, but lasted for only a short time. From a numerical perspective, the disturbance caused by machine round-off error (which corresponds to the inevitable experimental perturbations) triggers the transition of the configuration to its stable equilibrium state, i.e., the concentric shells. While ion drag and shielded Coulomb forces push them radially outwards, particles in one horizontal layer experience a compressive radial electric force. The cluster size appears to be a function of both N_p (number of dust particles) and a_p, in addition to the plasma operating conditions. A larger number (via more interactions) or size (through greater negative charge) of the particles leads to more intense repulsive forces among the particles and hence the cluster expands radially. Besides, the outer shells structure is also affected by that of the inner shells. For example, the elliptical shape of the outer shell in the (2,7) and (2,8) arrangements is due to the elongation caused by the two inner particles. In our numerical experimentation, we also realized that depending on the number of particles involved, the final solution may vary with different initial conditions. This is apparent from the difference of the shells structure in the case of $N_p=17$ between our result (1,5,11) and that of the experiment (1,6,10). Such disagreements in particles arrangement can also be observed by comparison of experimental studies of Thomas *et al.* [1] and Juan *et al.* [2] for $N_p=16$ and 17. The disaccord is ascribed to the existence of a number of local minima, with energies very close to the global minimum in the potential energy as a function of different possible configurations [59].

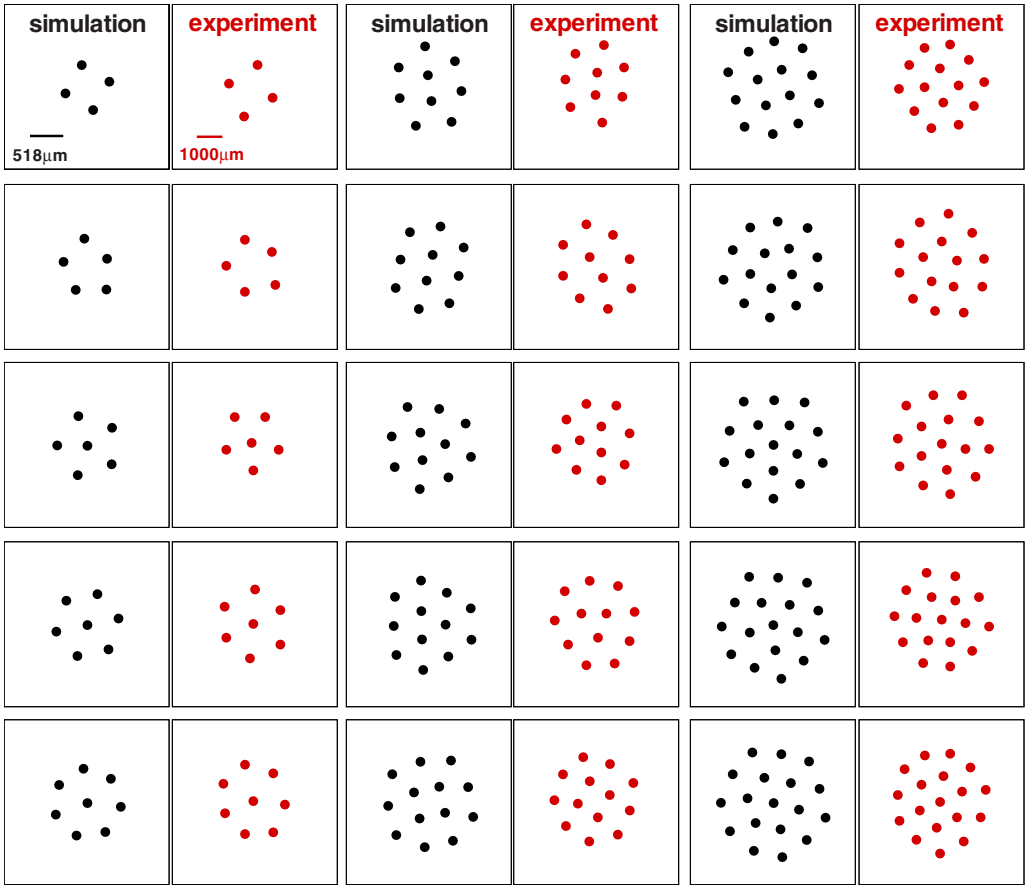

FIG. 5. (Color online) Top view of 2D Coulomb clusters for 4–18 melamine formaldehyde particles with $a_p=1.0$ μm, $f=f'=0.65$. Comparison of the results of the present study (odd columns) with the experiment of Thomas *et al.* [1] (even columns).

As previous investigators [22,23] have pointed out, owing to the competition between the repulsive and attractive forces, vertical correlation of the particles depends strongly on their sizes which in turn determine their vertical separation. Particles with sizes of large difference (e.g., 0.2 and 1.0 μm), would not 'feel' each other due to the large spacing, and thus both eventually sit at the center of their corresponding potential wells (which are located on the reactor axis) with the larger particle located at a lower height from the bottom electrode. On the contrary, for fixed model parameters, if the particles sizes are too close (e.g., 0.6 and 1.0 μm) the repulsive force might dominate over the attractive forces, and the pair remains vertically nonaligned. Therefore to demonstrate the model's ability to simulate the effect of ion streaming, first we investigate the interaction between two particles with painstakingly chosen radii 0.3 and 1.0 μm, and model parameters $f=0.3$ and $f'=0.45$. When all the interactions but the monopole-monopole force are turned off, and thus the ion focus effect is ignored, even with the reduced charge on the monopoles, particles form a radially offset pair, as displayed in Fig. 6(a). The magnitude of the screened Coulomb force, i.e., F_{mn}^{MM} in Eq. (32), is an ever-increasing function with respect to λ_D^n. Therefore the repulsive force on the upper particle appears greater in magnitude than that on the lower particle, since approaching the electrodes the local effective Debye radius increases, as revealed by Fig. 5(b) of Ref. [27]. As a result and in accord with the numerical findings of Vyas and Kushner [23], the lower particle pushes the upper away from the center of the confining potential. Figure 6(b) shows the side view of the particles equilibrium positions when all the interactions in the model are taken into account. A vertically aligned pair is formed due to the attractive forces involved in the interaction between the particles.

The current reactor lacks on the lower electrode a dc bias voltage and/or a strong confining geometrical (and hence potential) configuration such as a depression or a ring. Additionally, according to Fig. 7(c) of Ref. [27], there exist somewhat symmetrical (with respect to the center of the reactor) potential energy curves for the particles with radii in the above range. Consequently, even though the first layer is formed in the vicinity of the lower electrode, a larger number of similar particles would tend to form the second layer around the potential well located in the top side of the reactor. Particles motion from the proximity of the bottom electrode is initiated by the action of the repulsive force on them from the other particles. For the above reasons and in order to keep valid the assumption of one-way coupling of the plasma and particle phases and also drastically reduce the computational time, we restrict ourselves to two sets of ten particles with different sizes (i.e., $a_p=0.3$ and 1.0 μm) to simulate a double layer structure with $f=f'=0.65$. These 20

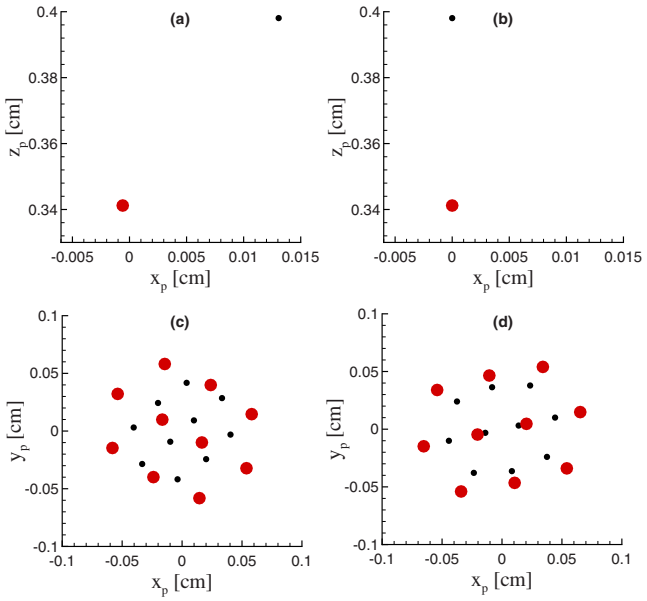

FIG. 6. (Color online) Side views of positions of two particles with radii a_p=0.3 μm (small black filled circle) and 1.0 μm (large red filled circle), f=0.3, f'=0.45, (a) with only monopole-monopole interaction, and (b) with all the interactions included. Top view of equilibrium configuration of ten a_p=0.3 μm (small black filled circles) and ten a_p=1.0 μm particles (large red filled circles), f=f'=0.65, (c) without, and (d) with ion focus effect.

particles with zero charge and velocity are simultaneously released from a circle with radius 0.1 cm at the top electrode. Within the sheath of the lower electrode, as a consequence of disparity in particles sizes, they segregate into two layers each with the expected shell structure of a monolayer constituted by ten particles. As illustrated by Fig. 6(c), excluding the dipole-involving interactions is conducive to nonvertically aligned orientation of the particles forming a haphazard structure seen from the top. In contrast, when the ion focus effect is intromitted particles tend to arrange themselves in a vertically ordered fashion [see Fig. 6(d)]. The reason of the slight vertical misalignment observed in Fig. 6(d) is twofold. First, farther from the reactor axis the ion velocity is no longer strictly vertical and it gains a radial component. Thus the ion focus region is not located directly beneath the particles and the resulting dipoles are titled. More importantly, larger particles which are placed in the lower layer acquire more negative charge, repel one another more, and form a more expanded structure than that assumed by the smaller upper particles. We postulate the latter effect of the particles having different sizes to be more pronounced than that of the radially varying fields in a rather small (<0.045 cm) radial stretch of the upper particles. In the relevant experiment of Refs. [11,50], a vertically adjusted multilayer structure is constructed by using a large count of same-sized particles. Furthermore, the plasma is more homogenous in the radial direction due to the use of a parallel plate geometry with electrode diameter considerably larger than the one considered here (i.e., 22 cm versus 2 cm). The above discussion provides a possible explanation why layers align upright in the pertinent experiments (see Figs. 1 in Ref. [9], 3(b) in Ref. [10], and 1 in Ref. [11]), whereas in our simulation a slight vertical disorder between the layers is observed. Last but not least, note that the dilute particle phase is not eventually densely packed since the interlayer distance amounts to 566 μm, while the local Debye length is 102 μm in the upper layer (with an average interparticle distance of 340 μm) and 157 μm in the lower layer (with an average interparticle distance of 480 μm), which is equivalent to k=4.37, 3.33, and 3.06 for interlayer, upper, and lower interparticle lattice parameters, respectively.

V. CONCLUSIONS

Numerical simulation of a particle-laden plasma flow within a capacitively coupled rf plasma reactor with cylindrical geometry is carried out. Boundary conditions which closely reflect the physics of the plasma particles transport are applied both on the electrodes and the surrounding dielectric wall surface. One-way coupling of the particle phase to the plasma phase is performed using a three-dimensional Lagrangian approach taking various forces acting on the particles into consideration. Details of a numerically tractable model for interaction of particles via ion focusing phenomenon is presented. Simulation results of spatial distribution of the particles of the same size at their equilibrium state show excellent qualitative agreement with experiments. In the framework of multilayer structures formed by the collective application of the competitory repulsive and attractive forces on a particle in one layer by all the particles of the other layer, the ability of the proposed model to vertically align the particles is verified. Determination of exact dependence of the model parameters on various variables such as degree of collisionality, local ion velocity, and particle charge remains an open issue for future investigations.

ACKNOWLEDGMENTS

This work was supported by Grant No. CBET-0651362 from the U.S. National Science Foundation.

[1] H. M. Thomas, J. Goree, A. Ivlev, U. Konopka, G. E. Morfill, L. Ratke, H. Rothermel, and M. Zuzik, *Proceedings of the Spacebound 2000 Conference, Vancouver*, 2001, pp. 1–6.
[2] W. Juan, J. Hsu, Z. Huang, Y. Lai, and L. I, Chin. J. Phys. (Taipei) **37**, 184 (1999).
[3] H. Ikezi, Phys. Fluids **29**, 1764 (1986).
[4] H. Thomas, G. E. Morfill, V. Demmel, J. Goree, B. Feuerbacher, and D. Mohlmann, Phys. Rev. Lett. **73**, 652 (1994).
[5] V. A. Schweigert, V. M. Bedanov, I. V. Schweigert, A. Melzer, A. Homann, and A. Piel, J. Exp. Theor. Phys. **88**, 482 (1999).

[6] M. Zuzic, A. V. Ivlev, J. Goree, G. E. Morfill, H. M. Thomas, H. Rothermel, U. Konopka, R. Sutterlin, and D. D. Goldbeck, Phys. Rev. Lett. **85**, 4064 (2000).
[7] J. H. Chu, and L. I, Phys. Rev. Lett. **72**, 4009 (1994).
[8] J. B. Pieper, J. Goree, and R. A. Quinn, J. Vac. Sci. Technol. A **14**, 652 (1996).
[9] K. Takahashi, T. Oishi, K. Shimomai, Y. Hayashi, and S. Nishino, Phys. Rev. E **58**, 7805 (1998).
[10] G. E. Morfill, and H. Thomas, J. Vac. Sci. Technol. A **14**, 490 (1996).
[11] A. Melzer, V. A. Schweigert, I. V. Schweigert, A. Homann, S. Peters, and A. Piel, Phys. Rev. E **54**, R46 (1996).
[12] O. Havnes, T. K. Aanesen, and F. Melandso, J. Geophys. Res. **95**, 6581 (1990).
[13] O. Havnes, G. E. Morfill, and C. K. Goertz, J. Geophys. Res. **89**, 10999 (1984).
[14] J. Goree, Plasma Sources Sci. Technol. **3**, 400 (1994).
[15] F. Melandso, and J. Goree, Phys. Rev. E **52**, 5312 (1995).
[16] M. Nambu, S. V. Vladimirov, and P. K. Shukla, Phys. Lett. A **203**, 40 (1995).
[17] D. P. Resendes, J. T. Mendonca, and P. K. Shukla, Phys. Lett. A **239**, 181 (1998).
[18] V. A. Schweigert, I. V. Schweigert, A. Melzer, A. Homann, and A. Piel, Phys. Rev. E **54**, 4155 (1996).
[19] V. A. Schweigert, I. V. Schweigert, A. Melzer, A. Homann, and A. Piel, Phys. Rev. Lett. **80**, 5345 (1998).
[20] A. V. Ivlev, and G. Morfill, Phys. Rev. E **63**, 016409 (2000).
[21] V. Steinberg, R. Sutterlin, A. V. Ivlev, and G. E. Morfill, Phys. Rev. Lett. **86**, 4540 (2001).
[22] G. A. Hebner, and M. E. Riley, Phys. Rev. E **69**, 026405 (2004).
[23] V. Vyas, and M. J. Kushner, J. Appl. Phys. **97**, 043303 (2005).
[24] V. V. Yaroshenko, H. M. Thomas, and G. E. Morfill, New J. Phys. **8**, 54 (2006).
[25] V. V. Yaroshenko, B. M. Annaratone, T. Antonova, H. M. Thomas, and G. E. Morfill, New J. Phys. **8**, 203 (2006).
[26] J. Cao, and T. Matsoukas, J. Appl. Phys. **92**, 2916 (2002).
[27] M. Davoudabadi, and F. Mashayek, Phys. Plasmas **12**, 073505 (2005).
[28] M. Davoudabadi, B. Rovagnati, and F. Mashayek, IEEE Trans. Plasma Sci. **34**, 142 (2006).
[29] M. Davoudabadi, and F. Mashayek, J. Appl. Phys. **100**, 083302 (2006).
[30] B. Rovagnati, M. Davoudabadi, G. Lapenta, and F. Mashayek, J. Appl. Phys. **102**, 073302 (2007).
[31] M. Davoudabadi, B. Rovagnati, and F. Mashayek, *43rd AIAA Aerospace Sciences Meeting and Exhibit, Reno, Nevada, 2007*, AIAA, paper no. 2007-0790.
[32] J. E. Hammerberg, D. S. Lemons, M. S. Murillo, and D. Winske, IEEE Trans. Plasma Sci. **29**, 247 (2001).
[33] G. Joyce, M. Lampe, and G. Ganguli, IEEE Trans. Plasma Sci. **29**, 238 (2001).
[34] H. C. Kim, and V. I. Manousiouthakis, J. Appl. Phys. **89**, 34 (2001).
[35] J. P. Boeuf, Phys. Rev. E **36**, 2782 (1987).
[36] J. P. Boeuf, and L. C. Pitchford, Phys. Rev. E **51**, 1376 (1995).
[37] E. Suetomi, M. Tanaka, S. Kamiya, S. Hayashi, S. Ikeda, H. Sugawara, and Y. Sakai, Comput. Phys. Commun. **125**, 60 (2000).
[38] H. Goldstein, P. Charles, and J. Safko, *Classical Mechanics*, 3rd ed. (Addison-Wesley, San Francisco, 2002).
[39] M. Davoudabadi, and F. Mashayek, *Abstract Book of the 33rd IEEE International Conference on Plasma Science, Traverse City, MI, 2006* (IEEE, New York, 2006).
[40] S. J. Choi, and M. J. Kushner, J. Appl. Phys. **75**, 3351 (1994).
[41] M. S. Barnes, J. H. Keller, J. C. Forster, J. A. O'Neill, and D. K. Coultas, Phys. Rev. Lett. **68**, 313 (1992).
[42] I. H. Hutchinson, and L. Patacchini, Phys. Plasmas **14**, 013505 (2007).
[43] S. A. Khrapak, S. V. Ratynskaia, A. V. Zobnin, A. D. Usachev, V. V. Yaroshenko, M. H. Thoma, M. Kretschmer, H. Höfner, G. E. Morfill, O. F. Petrov, and V. E. Fortov, Phys. Rev. E **72**, 016406 (2005).
[44] J. E. Daugherty, and D. B. Graves, J. Appl. Phys. **78**, 2279 (1995).
[45] J. E. Daugherty, R. K. Porteous, and D. B. Graves, J. Appl. Phys. **73**, 1617 (1993).
[46] S. A. Khrapak, A. V. Ivlev, G. E. Morfill, and H. M. Thomas, Phys. Rev. E **66**, 046414 (2002).
[47] C. Zafiu, A. Melzer, and A. Piel, Phys. Plasmas **10**, 1278 (2003).
[48] C. Zafiu, A. Melzer, and A. Piel, Phys. Plasmas **10**, 4582 (2003).
[49] P. K. Shukla, and A. A. Mamnun, *Introduction to Dusty Plasma Physics* (IOP Publishing, London, 2002).
[50] T. Trottenberg, A. Melzer, and A. Piel, Plasma Sources Sci. Technol. **4**, 450 (1995).
[51] A. Melzer, V. A. Schweigert, and A. Piel, Phys. Rev. Lett. **83**, 3194 (1999).
[52] H. C. Lee, D. Y. Chen, and B. Rosenstein, Phys. Rev. E **56**, 4596 (1997).
[53] D. P. Resendes, Phys. Rev. E **61**, 793 (2000).
[54] G. Lapenta, Phys. Scr. **64**, 599 (2001).
[55] G. Lapenta, Phys. Rev. Lett. **75**, 4409 (1995).
[56] G. Lapenta, and J. U. Brackbill, Phys. Scr., T **T75**, 264 (1998).
[57] J. D. Jackson, *Classical Electrodynamics*, 3rd ed. (Wiley, New York, 1999).
[58] A. Allievi and R. Bermejo, J. Comput. Phys. **132**, 157 (1997).
[59] V. M. Bedanov, and F. M. Peeters, Phys. Rev. B **49**, 2667 (1994).